Flow (2026), **6** E25
doi:10.1017/flo.2026.10063

FLOW CAMBRIDGE UNIVERSITY PRESS

RESEARCH ARTICLE

Turbulent flow past idealised arrays of photovoltaic panels: an experimental study

Pier Giuseppe Ledda, Maria Grazia Badas and Giorgio Querzoli

DICAAR, Università degli Studi di Cagliari, Via Marengo 2, Cagliari 09123, Italy
Corresponding author: Giorgio Querzoli; Email: giorgio.querzoli@unica.it

Received: 23 January 2026 UTC; **Revised:** 23 June 2026 UTC; **Accepted:** 25 June 2026 UTC

Keywords: canopy flow; dispersion; particle image velocimetry; photovoltaic panels; ventilation

Abstract
We experimentally investigated the turbulent flow in a water channel developing past a two-dimensional array of photovoltaic panels, with varying incidence angle and spacing. Particle image velocimetry revealed two distinct regimes, depending on the incidence angle, while the dependence on inter-panel spacing was weaker. Positive incidence angles produce high turbulence and intense transport above the panels, with strong mixing between the canopy and the external flow. Conversely, negative incidence angles yield a skimming flow with large recirculation vortices that dominate the canopy layer. Vertical profiles, ventilation rates and turbulent statistics indicate that even a modest positive incidence significantly enhances ventilation and scalar transport, whereas they are substantially lower in the case of negative incidence. A Lagrangian analysis using synthetic passive particles allowed the estimation of the residence times and turbulent dispersion coefficients. The latter were more than an order of magnitude larger for positive than for negative incidence. The results demonstrate how panel configuration changes mixing and dispersion processes, providing a fluid mechanics basis for refined microclimate models useful for guiding the design of advanced photovoltaic farms.

Impact Statement
The growing installation of large-scale photovoltaic farms in rural landscapes calls for a better understanding of the fluid dynamics processes at play. Large-scale farms alter the local microclimate and near-ground turbulence, yet design tools still treat convective and scalar exchange with approximated laws based on simplified arguments. We report controlled water-channel experiments of turbulent flow past idealised arrays of photovoltaic panels, varying tilt and inter-row spacing typical of photovoltaic and agrivoltaic layouts, quantified with time-resolved image velocimetry. Two regimes emerge: positive incidence induces energetic, highly turbulent, shear layers and coherent transport over the panels, greatly increasing dispersion. Conversely, negative incidence yields a skimming-flow state with canyon-like recirculation with weak turbulence penetration, low exchange and longer tracer residence times. This work aims to inspire improved parameterisations for fluid dynamics models and give insight into the effect of panel orientation and spacing to manage microclimate and transport.

1. Introduction

The rapid expansion of photovoltaic farms in rural landscapes, driven by the global transition to renewable energy, presents fluid mechanical challenges as far as it affects local microclimate and agricultural production (Glick *et al*. 2020*a*). Photovoltaic panels are usually arranged in parallel rows of rectangular panels, which may rotate along one or two axes to track the sun, with the one-axis configuration being the most common choice as the best compromise between cost and productivity (Huld *et al.* 2010). This layout creates a repetitive quasi-two-dimensional canopy of parallel rectangular thin panels, which affects the near-ground airflow and influences the large-scale structures of the atmospheric boundary layer. Consisting of a series of periodic obstacles, photovoltaic farms have geometrical features in common with the widely investigated urban canyons (Di Bernardino *et al*. 2015; Oke 1988). The turbulence promoted by the photovoltaic canopy alters the exchanges of heat, moisture and momentum between the soil and the atmosphere, which are critical for defining the microclimatic conditions, in turn crucial for crop development (Britter & Hanna 2003).

As in urban environments, the presence of the panels alters the heat balance at the ground (Barron-Gafford *et al*. 2016). In recent years, photovoltaic plants have evolved from their traditional design, which focuses on maximising energy production, to agrivoltaic systems that promote a synergistic relationship between energy and agricultural production. While in the first case, panels cover almost the entire available area, preventing any other use of the soil, in the second case, the panels are arranged to allow agricultural production underneath them (Dinesh & Pearce 2016; Dupraz *et al*. 2011). To grant an effective agricultural development underneath the panels, it is important to evaluate local heat transfer, evapotranspiration rates and vertical moisture transport, ultimately influencing the microclimate, hydrological balance, and eventually the crop growth. These processes are all driven by turbulent fluxes within the atmospheric boundary layer. Therefore, understanding the fluid mechanics induced by photovoltaic farm layouts is essential for evaluating their environmental impact and for guiding sustainable deployment through robust engineering frameworks. Since photovoltaic panels' efficiency depends on their temperature, most of the previous research has focused on performing integral energy balances between the panels, the ground and the surrounding air, while accounting for solar radiation (Heusinger *et al*. 2020; Li *et al*. 2024). However, employed convective heat transfer models remain approximate (Vigiak *et al*. 2003): although they reasonably capture the order of magnitude of heat exchange with the air, they do not account for the effects of panel inclination and inter-row spacing, i.e., geometrical factors that drive turbulence structure in canopy flow scalar exchanges (Fellini *et al*. 2020, 2021; Fernando *et al*. 2001).

Improving current models and reducing the need for empirical calibration requires a strong fluid mechanical foundation. Flow past a series of idealised obstacles in the urban environment (Husain *et al*. 2013; Song & Wang 2015; Soulhac *et al*. 2011) has been investigated in different configurations, including both two-dimensional, such as arrays of aligned prisms orthogonal to the flow (Badas *et al*. 2017; Di Bernardino *et al*. 2015; Garau *et al*. 2018), and three-dimensional arrays of cubic or prismatic obstacles (Di Bernardino *et al*. 2020a; MacDonald *et al*. 1997). Systematic studies of idealised, periodic urban canyons have allowed researchers to explore the effects of roughness aspect ratio, roof geometry and spacing on mean-flow structure and turbulent exchange processes (Bentham & Britter 2003; Macdonald *et al*. 1998; Reynolds & Castro 2008; Simón-Moral *et al*. 2014). As a rule of thumb, depending on building height, width and inter-building spacing, three canonical flow regimes are generally observed (Ngan & Lo 2016; Oke 1988), each driving different mixing and ventilation processes. Densely packed configurations produce skimming flow, where one or more recirculation regions develop within the canyon, and ventilation remains weak. At intermediate spacings, wake interference occurs, as the wakes of successive buildings interact, generating high unsteadiness and turbulence within the canyon. For sufficiently large spacings, an isolated roughness flow regime develops, with large wake structures that dissipate before reaching downstream obstacles. These flow regimes strongly affect the transport of pollutants or temperature, among others. Studies of idealised urban canyons have thus been crucial for identifying the physical mechanisms governing ventilation, heat transfer and scalar dispersion. Photovoltaic roughness elements, however, are typically smaller and differ from urban buildings because they are not sealed at the bottom, allowing a flow between adjacent canyons. Furthermore, panels are thin plates rather than bluff bodies such as buildings. Therefore, the fluid–structure interaction is the one typical of airfoils, and the incidence angle significantly affects the flow (Glick *et al*. 2020*a*), also at small angles. Experimental and numerical studies have focused on two-dimensional photovoltaic canopies. Glick *et al*. (2020*a*) proposed a simplified classification of three flow regimes: at large negative incidence (we define the incidence angle as positive when the incoming flow impacts the lower panel surface, and *vice versa*, according to the airfoil convention) large recirculation regions develop within the canopy; at low incidence, two streams of different velocities develop above and below the panels; at large positive incidence, turbulence is concentrated over the upper panel surfaces, promoting turbulent fluxes and ventilation.

Experiments demonstrated a marked increase in the heat transfer coefficient for large positive incidence (Glick *et al*. 2020*a*, *b*). Smith *et al*. (2022) observed that increasing panel height enhances the heat transfer coefficient. However, their experimental set-up did not allow the investigation of large regions around the panels. Stanislawski *et al*. (2022), using large-eddy simulations with a single incidence, showed that larger inter-panel distances enhance the overall cooling of the panels. While previous studies have mainly addressed the panel thermal performances (Glick *et al*. 2020*a*, *b*; Smith *et al*. 2022), the flow spatial organisation within and immediately above the panels remains largely unexplored. This is crucial since, in agrivoltaics, there is no universal optimum corresponding to either maximising or minimising ventilation and scalar exchange, with the desirable regime depending on a wide range of factors, such as meteorological conditions, crop type and management objectives (Barron-Gafford *et al*. 2016; Dupraz *et al*. 2011).

The present study focuses on the inter-panel velocity field spatial structure and on the vertical exchange across the canopy top, mechanisms that are directly relevant to the control of agrivoltaic microclimate. We investigate the complete velocity field around the panels at high spatial and temporal resolution for a wide range of configurations, which can serve to shed new light on the mechanisms driving turbulence and scalar mixing in the photovoltaic canopy. To achieve this, we used transparent model panels allowing full particle image velocimetry (PIV) beneath and around the panels. We varied both the spacing and pitch of the panels. The present experiments are restricted to neutral conditions and do not include buoyancy effects. This choice is intended to isolate the mechanically driven transport mechanisms and provide a controlled reference case before introducing thermal coupling (Zhao *et al*. 2020), which in turn may quantitatively modify the scenario, especially under strong radiation and weak wind conditions, without altering the overall picture (Mouzourides *et al*. 2022; Zhao *et al*. 2021).

The paper is organised as follows. Section 2 describes the experimental apparatus and methodology. Section 3 examines the mean-flow structures that develop in the canyon as a function of panel incidence and spacing. Section 4 quantifies turbulent statistics and the mean exchange rates across the canopy. Eventually, Section 5 investigates passive tracer transport through the instantaneous flow of synthetic particles across and above the canopy, relating the resulting dispersion to both mean and turbulent flow properties.

2. Methods: experimental set-up

The experimental apparatus is sketched in figure 1. Laboratory experiments were performed in a water channel 8.00 m in length, $L_y = 0.40$ m in width, with a water depth of $H_w = 0.50$ m, already employed for urban canyon studies (Garau *et al*. 2018). A constant flow rate was imposed by a closed loop, and water depth was tuned by means of a sharp-crested weir downstream of the channel. A 0.10 m-thick honeycomb acted as a flow straightener at the inlet of the channel. It was followed by irregularly distributed pebbles (≈5 mm in diameter) along 2 m of the bottom of the channel to promote the development of a fully turbulent boundary layer upstream of the array of panels (Badas *et al*. 2020). The model farm consisted of an array of 20 equidistant and transparent polycarbonate rectangular panels, 1.5 mm thick and $L = 30.0$ mm wide, spanning the whole channel width. To minimise undesired light diffusion, the panels were painted black except in the vicinity of the mid-section of the channel, where they were transparent, to allow the whole area around the panels to be illuminated. Furthermore, they were glued to steel shafts (≈2 mm in diameter), hinged at their lateral ends at a height $h = 25$ mm. Set screws allowed the panels' pitch to be locked at the prescribed angle. We denote the streamwise and vertical directions by x and z, respectively, with their origin at the ground in the middle of the space between the two panels delimiting the investigated periodic unit. The uniform panel orientation was guaranteed via specific templates, removed after locking the screw before the experiment. With the flow from left to right, the panel tilt

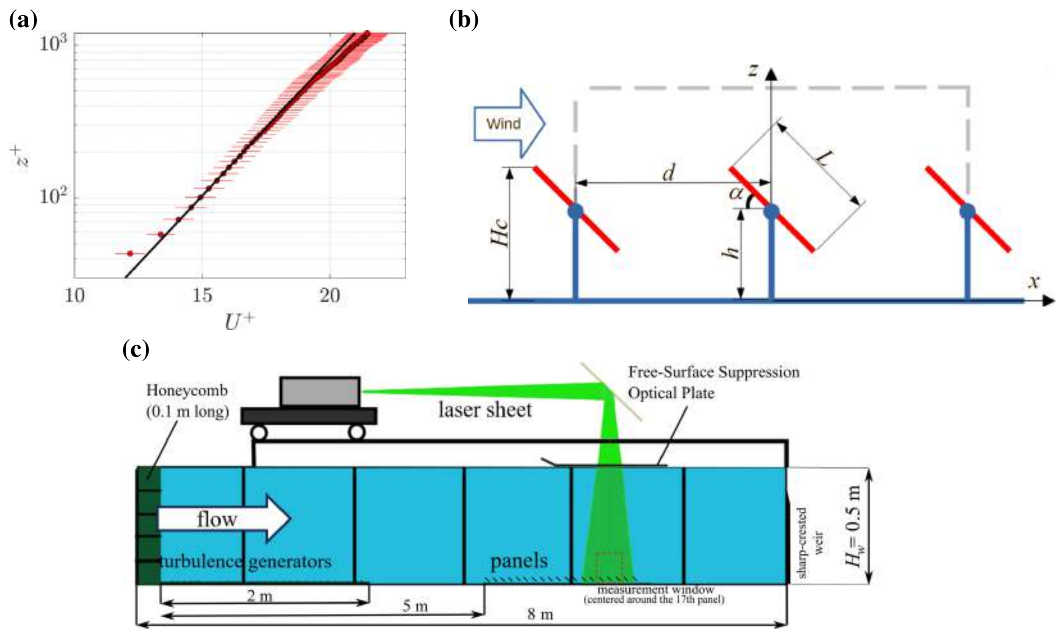

Figure 1. *(a) Horizontal incoming mean velocity profile along the centreline, in inner variables: experiments with uncertainty (red dots) and logarithmic fit in the region 100 < z^+ < 300 (black line). The uncertainty bar width is two standard deviations. (b) Sketch of a periodic unit of the canopy framed in grey with its geometrical parameters. (c) Water channel with elements of the experimental apparatus.*

angle, α, is defined as positive when rotation is clockwise, and negative when rotation is counterclockwise. We considered two spacing distances d between the panels, yielding inter-panel aspect ratios of $AR = d/L = 5/3 \approx 1.67$ and $AR = 10/3 \approx 3.33$. The first mimics a classical photovoltaic farm with packed panels (dense configuration), whereas the second mimics an agrivoltaic farm with a larger distance to allow for agricultural activities (sparse configuration).

In the present geometry, the canopy height $H_c = h + L/2\ \sin(\alpha)$ is approximately 30 mm. The logarithmic fit of the incoming boundary-layer profile in figure 1a was performed in inner variables, i.e., $U^+ = \ln(z^+)/\kappa + B$ (with $U^+ = U/u_*$,U the streamwise velocity, $\kappa = 0.41$, $z^+ = z\,u_*/\nu$, and B an additive constant), at each streamwise location over the range $100 < z^+ < 300$, i.e., where the log law is typically assumed to be valid. The analysis yields $u_* = 11.4 \pm 0.4$ mm s^{-1}, where the uncertainty denotes the standard deviation across streamwise locations. The corresponding roughness length, evaluated through $z_0 = (\nu/u_*)\exp(-\kappa B)$, is $z_0 = 20 \times 10^{-3} \pm 5 \times 10^{-3}$ mm, i.e., $z_0 \approx 10^{-3} H_c$, in line with previous studies (Badas *et al*. 2020). The difference between data and logarithmic fit remains within 2.5% within the whole investigated height range ($z^+ < 1300$). Furthermore, the ratios between canopy height and channel length scales $H_c/H_w \approx 0.06$ and $H_c/L_y \approx 0.075$ are comparable to previous water-channel studies of two-dimensional obstacle arrays, suggesting that blockage effects in the investigated region are limited. Based on figure 1a, the incoming inner boundary-layer thickness is approximately $\delta \approx 0.1$ m, so that $H_c \approx 0.3\delta$. Therefore the canopy is fully embedded within the incoming boundary layer, and the measurement focus is on the roughness-sublayer region (Di Bernardino *et al*. 2015). These fluid dynamic and geometrical conditions are in line with other previous studies (Badas *et al*. 2020; Di Bernardino *et al*. 2015; Garau *et al*. 2018).

We exploited the geometrical symmetry of the system, analysing the flow in the vertical channel mid-plane (x–z) (Badas *et al*. 2020). Non-buoyant particles (pine pollen) dispersed in water were illuminated on the measuring plane by a 2 mm-thick light sheet, generated by a diode laser and projected from above through a transparent optically rectified glass carefully placed just at the water surface above the investigation region. The plate was 1.5 m long, equipped with a smooth leading edge and carefully held aligned with the free surface, so as not to generate disturbances in the subcritical flume either upstream or downstream. Consequently, in the measurement region, the depth was constant, and the flow above the canopy was not open channel. A high-speed camera (2240×1740 pixels in resolution), placed perpendicular to the interrogation area, recorded 330 frames per second on a SSD disk array without compression. Following previous water-channel studies of periodic two-dimensional obstacle arrays, the measurement region was located at the 17th periodic unit, allowing the boundary layer and the canopy-top shear layer to fully develop over the sixteen upstream panels, as observed in similar canopy flows, see e.g. Badas *et al*. (2020). Images were analysed via a feature-tracking velocimetry technique. Seeding particles were identified via the Harris corner detection algorithm. Displacements between successive frames were computed by comparison of interrogation windows (17×17 pixels) and by minimising the dissimilarity measured by a Lorentzian estimator (Besalduch *et al*. 2013). Particle velocities were obtained by dividing the displacements by the corresponding interframe time interval. Velocities were made non-dimensional with the average free-stream velocity, $U \approx 0.24$ m s^{-1}, of each experiment. The Reynolds number based on the panel length, L, $Re = UL/\nu$, is approximately 7,000 ($\nu = 10^{-6}$ m^2 s^{-1} indicates the kinematic viscosity of the water). Conversely, using the incoming mean velocity at canopy height, $U(H_c)$, we obtain $Re_{Hc} = UH_c/\nu \approx 7{,}000$, while the friction Reynolds number is $Re_\tau = u_* H_c/\nu \approx 342$. These values place the flow in a turbulent regime typically considered for experimental water-channel studies in urban-canopy flows, where Reynolds number effects have been reported to be small enough so that the main flow features are captured (Badas *et al*. 2020; Britter & Hanna 2003; Di Bernardino *et al*. 2015, 2020*a*; Uehara *et al*. 2003). Furthermore, Uehara *et al*. (2003) proposed also to verify that the region in which $z^+ < 20$ was limited, in our case, $z < 1.8$ mm $\approx 0.1 H_c$. We then evaluated the mean velocity field and the turbulence statistics by averaging instantaneous sparse velocity samples obtained from 10,000 velocity fields, corresponding to approximately 30 s, i.e. approximately 240 advective time scales (L/U), on a 97×131 regular grid. Convergence of second-order statistics was checked by comparing turbulent kinetic energy (TKE) and Reynolds-stress profiles obtained from progressively increasing subsets of the ensemble. The profiles were found to be stable for the full set of 10 000 fields, with residual statistical non-dimensional uncertainty below 10^{-3} in all of the cases.

3. Mean-flow general structure

Figure 2 shows the streamlines and magnitude of the mean velocity field for the dense array of panels ($AR = 5/3$). We begin with the positive incidence cases. At a small incidence ($\alpha = 20°$, figure 2a), the velocity field shows the typical characteristics of the flow around a flat plate (Smith *et al*. 2021). The streamlines follow the panel, with a small recirculation on the upper surface, close to the leading edge (denoted as **a** in figure 2). The flow is accelerated in the convergent space between the panel and the ground, reaching its highest velocity where the gap is the narrowest (so-called *vena contracta*). Downstream of it, the flow decelerates and deflects upwards to impinge on the lower surface of the following panel, close to the leading edge, as is typical of the flow around flat airfoils. Subsequently, an intense, continuous streamwise flow also develops below the panels. At the *vena contracta*, velocities comparable to the external flow are reached. At higher incidence angles ($\alpha = 40°$ and 55°, figures 2c and 2e), two additional vortical structures appear. The first, labelled **b**, develops at the trailing edge as the flow separates from the panel. The second, labelled **c**, is located downstream of the *vena contracta*, where the flow decelerates and is redirected upwards. This adverse-pressure-gradient region is strong enough to trigger separation from the ground. Above that structure, high-velocity fluid from the upper flow is redirected toward the lower surface of the downwind panel. The lower surface is therefore exposed to larger velocities compared with the upper surface, which may enhance advective heat exchange. The vortex **a** is still present and increases in size. In summary, at α = 20°, two intense continuous streams develop both above and below the panels. Conversely, at α = 40° and α = 55°, the inter-panel regions are dominated by recirculating structures, suggesting lower ventilation in the canopy layer.

We now focus on figures 2b, 2d and 2f, where the incidence is negative. Overall, low-velocity recirculations dominate close to the ground. Regardless of the tilt angle, the flow topologies are rather different

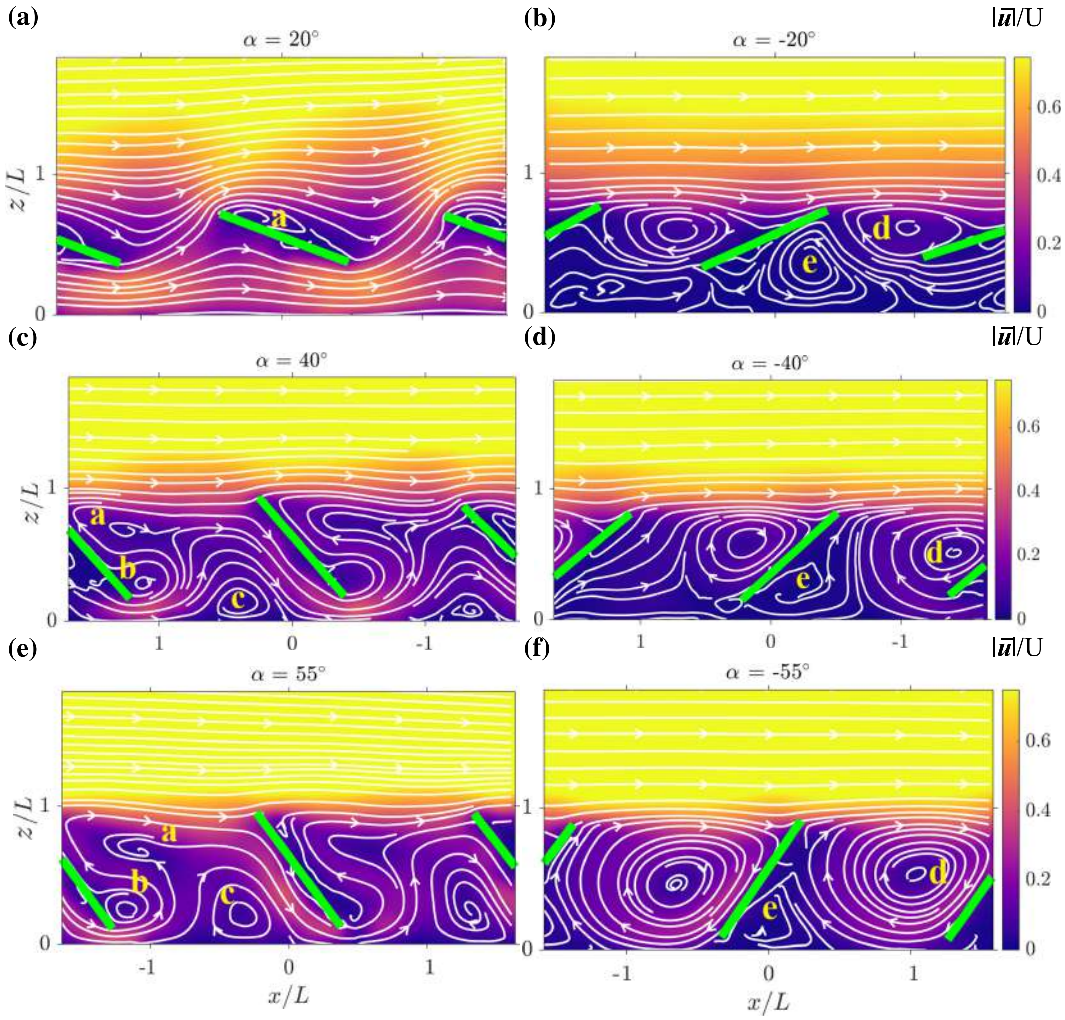

Figure 2. *Dense case (AR = 5/3): streamlines of the mean velocity field overlaid with colour maps of the mean velocity magnitude, for (a, c, e) positive and (b, d, f) negative incidence.*

from those in the positive incidence case. Specifically, two main vortical structures dominate: the first is a clockwise recirculating vortex (denoted as **d**) generated by the separation at the trailing edge of the panel, in the upper part of the canyon; the second vortex (denoted as **e**) is a counterclockwise-rotating recirculation generated by the counter-streamwise flow developing below the panels. As the incidence increases, the recirculating structure **d** grows and progressively invades the entire canyon, while the vortex **e** weakens accordingly (figures 2d and 2f). Flow structures described in figures 2b, 2d and 2f) are reminiscent of the skimming flow that develops in urban canyons. Specifically, for negative incidence angles, large portions of the ground surface are exposed to counter-streamwise flow, while canyons are dominated by recirculation structures, suggesting a weak contribution of the mean flow to the canopy layer ventilation. However, the case $\alpha = -55^\circ$ shows the highest velocity near the ground and panel upper surface due to the increased strength of the vortex **d**, suggesting the persistence of flow asymmetry due to the incidence angle.

Figure 3 shows the sparse panel configuration case ($AR = 10/3$). Overall, compared with the dense configuration, higher velocities are observed within the canopy. For moderate positive incidence ($\alpha = 20^\circ$ and $\alpha = 40^\circ$, figures 3a and 3c), the velocity field structures are similar to those observed in

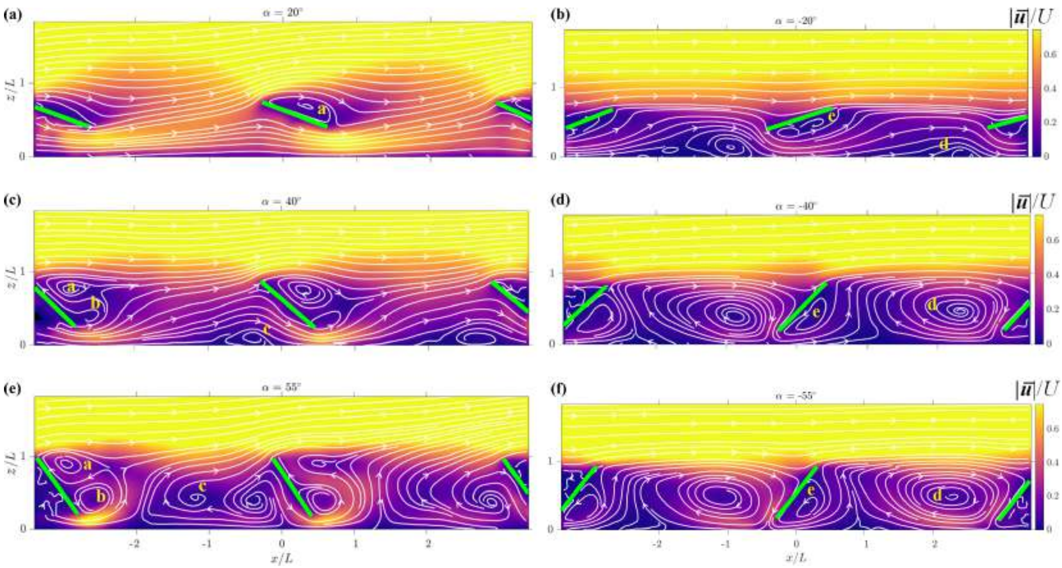

Figure 3. *Large distance case (AR = 10/3): streamlines of the mean velocity field overlaid with colour maps of the mean velocity magnitude, for (a, c, e) positive and (b, d, f) negative incidence.*

figure 2a. A continuous streamwise flow develops below the panels, which accelerates through the convergent gap below the panels and, again, impinges close to the leading edge of the downwind panel. However, the recirculation at the ground developing at $\alpha = 40^\circ$ (**c** in figure 3c) is smaller and velocities through the panel–ground gaps are of the same order as the external flow. The same phenomenon is anticipated and enhanced at the largest positive incidence, resulting in a recirculation occupying all the space left by the vortices at the upper surface of the upwind panel. Irrespective of the tilt angle, the recirculation region covers the entire upper surface of the panels even for $\alpha = 40^\circ$ and $\alpha = 55^\circ$, the separation occurs both at the leading and trailing edge, generating two counter-rotating vortices (figures 3c and 3e). This flow structure is reminiscent of the wake interference regime observed in urban canopies (Hunter *et al*. 1990). For $\alpha < 0$, similarly to the dense case, the flow within the canyon is dominated by a counterclockwise vortex (labelled as **e**) leeward of the panels and a clockwise vortex at the ground just upwind of the panels (labelled as **d**).

The analysis of the structures dominating the velocity field is leveraged to draw insights into the contribution of the mean flow to heat-exchange and transport processes occurring between the photovoltaic canopy and the overlying external flow. Low incidence angles result in the formation of a continuous streamwise flow under the panels, periodically accelerating and decelerating at velocity magnitudes comparable to those of the external flow. For positive incidence angles, the flow accelerates through the narrow gap beneath the panel and then decelerates, producing pressure recovery and upward deflection toward the lower surface of the following panel. For negative incidence, by contrast, the lower panel surface is mainly reached by fluid recirculating within the canopy, leading to weaker direct impingement and reduced mean-flow exchange. For large positive incidence ($\alpha = 40^\circ$ or $\alpha = 55^\circ$), the development of multiple recirculation bubbles induces strong vertical velocities that enhance fluid exchange across the canopy, thereby improving photovoltaic canopy ventilation and promoting the dispersion of scalars toward the outer flow that might otherwise be simply advected downstream near the ground. In contrast, large negative incidence angles ($\alpha = -40^\circ$ or $\alpha = -55^\circ$) lead to large recirculation regions within the canopy, with a limited exchange with the external roughness layer, and a general structure reminiscent of the skimming-flow regime, associated with little exchange between the canopy and the overlying layer (Oke 1988). This suggests a more intense advective mixing for positive than for negative incidence angles. Eventually, it is worth noting that the resulting mean velocity fields align with two-dimensional Reynolds Averaged Navier-Stokes (RANS) simulations of panel arrays at real scale (Ledda *et al*. 2024).

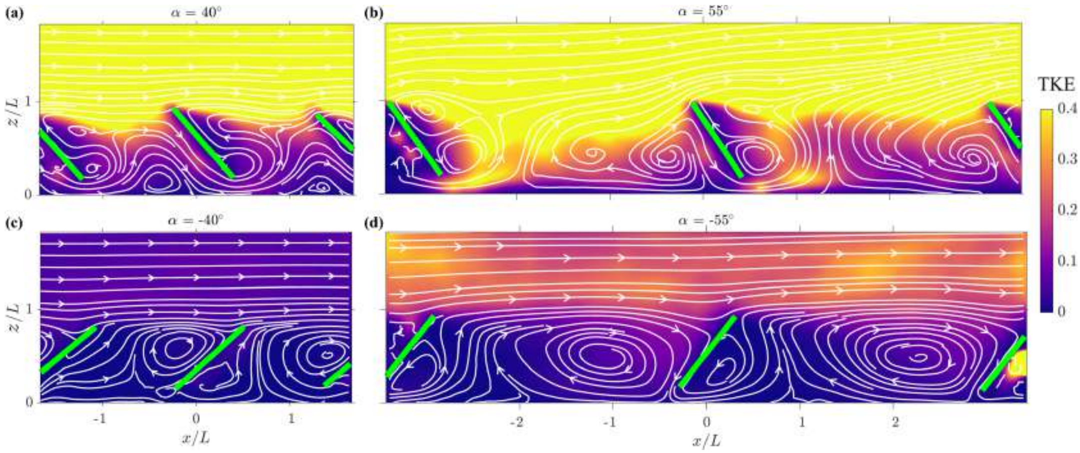

Figure 4. *Streamlines of the mean velocity overlaid with colour maps of the non-dimensional TKE. Left column (a, c): dense distribution case and $\alpha = \pm 40^\circ$. Right column (b, d) sparse distribution case and $\alpha = \pm 55^\circ$. Spatial coordinates are made non-dimensional by the panel length, L.*

4. Mixing and transport through turbulent statistics and integral indices

We next present the mechanisms of advection by the mean flow, mixing and dispersion that result from the interaction between photovoltaic roughness and the atmospheric boundary layer. These are the key elements to be considered in the design of an agrivoltaic farm to optimise the microclimate for agricultural and energy production.

4.1. Turbulent kinetic energy

The in-plane TKE, measured in the centreline vertical plane of the water channel under consideration, is $\mathrm{TKE} = \frac{1}{2}\left(\overline{u'^2} + \overline{w'^2}\right)/U^2$, where the overbar denotes the time average. The TKE plays a crucial role in dispersing scalars within and above the canopy. Figure 4 presents the TKE distributions for two large positive and negative incidence angles at both *AR* values. Notably, much higher TKE values within the canopy and roughness layers are observed when the incidence angle is positive. A closer look shows that, for positive incidence angles, relatively high TKE values are observed on the lower panel surfaces and in the decelerating flow downstream of the *vena contracta*. Conversely, for negative incidence, the skimming-like flow allows the penetration of relatively high TKE only in the downwind portion of the upper canyon interface, a region that linearly expands with the streamwise distance because of the developing instability of the shear layer.

The present results highlight the role played by the panels that interact with the incoming flow as flat airfoils actively deflecting the flow, rather than behaving as bluff bodies such as buildings or vegetation. Therefore, the canopy-top shear-layer dynamics is deeply affected by the incidence angle. For positive incidence angles, the interaction between the high-momentum outer flow and the low-momentum fluid from the canopy, ejected just upstream of the leading edge of the panel, promotes turbulence production and explains the elevated TKE observed in the overlying roughness sublayer and, in the sparse case, also within the canopy. The high-TKE regions observed in the sparse configuration downstream of the under-panel gap and near the lower panel surfaces are associated with flow upward deflection. For negative incidence angles, instead, the TKE maps depict a skimming-like regime dominated by large recirculation structures within the canopy. In this case, turbulence penetration is reduced, and high TKE remains mainly confined to the upper downwind portion of the canopy, with reduced interaction between canopy and outer flow.

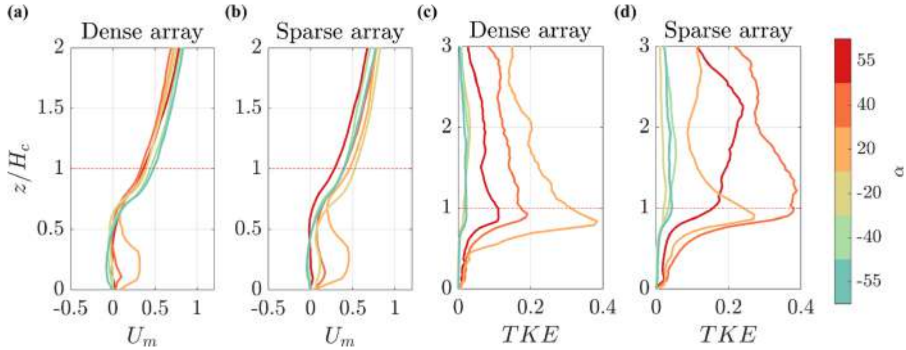

Figure 5. *Vertical profiles of the nondimensional horizontal velocity component horizontally averaged over the periodic unit,* U_m*, in the (a) dense and (b) sparse cases, and non-dimensional TKE for (c) dense and (d) sparse cases. Colour indicates the incidence angle according to the scale on the right.*

4.2. Horizontally averaged vertical profiles

We now summarise the above results into vertical profiles by horizontally averaging the quantities over a periodic unit. Figures 5a and 5b report the vertical profiles of the non-dimensional average horizontal velocity, U_m, which give an indication of both the streamwise advection driven by the mean flow and how the panels affect the structure of the atmospheric boundary layer. For $\alpha = 20^\circ$, a significant positive horizontal average velocity is observed in the lower canopy layer ($z < 0.5H_c$), and velocities attain values of approximately $U_m \cong 0.3$ for $0.1H_c < z < 0.3H_c$, independently of the panel distance. Nearly negligible positive velocities are observed for $z < 0.2H_c$, in the cases $\alpha = 40^\circ$ and $\alpha = 55^\circ$. For negative incidence ($\alpha = -40^\circ, -55^\circ$), the velocity is negative in the lower half of the canopy, suggesting a moderate upwind overall transport below the panels. However, at a height of approximately $0.7H_c$, the average horizontal velocity becomes positive, with a logarithmic increase. This height marks the transition between the lower recirculating region and the overlying streamwise flow (Di Bernardino *et al*. 2020*a*).

Figures 5c and 5d show the non-dimensional *TKE* horizontally averaged over the periodic unit for the dense and sparse panel cases. A positive incidence yields significantly high turbulence values that strongly depend on the incidence itself, whilst negative incidence is associated with a much lower *TKE* and correspondingly lower dependence on α, in agreement with figure 4. Specifically, irrespective of the panel spacing, negative incidence cases are characterised by low *TKE* values, which are almost negligible for $z < 0.7H_c$. Conversely, positive α is associated with a more turbulent flow, with the *TKE* being maximum at $z \simeq 0.8\ H_c$, where the interfacial shear layer develops. Similarly, in the dense case (figure 5c), a marked *TKE* peak occurs within the canopy at approximately $z = 0.8H_c$. This peak intensity diminishes markedly as the (positive) incidence increases. Increasing the distance (figure 5d) leads to very similar TKE values, although the turbulence propagates more above the canopy, in the roughness layer, for large and positive incidence. In these cases, reminiscent of the wake interference regime, the peak is no longer as marked as in the dense case.

In summary, the incidence has a notable effect on the *TKE* distribution across and above the canopy, not only on its spatial distribution, but also on its magnitude, due to the different interaction between the flow and the panels depending on the sign of the incidence. For negative incidence, the main flow above the canyon tends to skim over the canopy without deeply penetrating it, thus resulting in a dominant recirculating vortex confined within the canyon. Consequently, the interfacial velocity gradient is mitigated, preventing the development of a sharp shear layer. In this condition, the exchange between the canyon and the overlying flow is largely limited, consistently with the observed low *TKE* values. In contrast, for positive incidence, the recirculation vortices on the upper surface of the panels enhance the shear-layer intensity and the exchange between the near ground and the upper interface of the canopy and above the roughness layer, promoting the flow instability and increased turbulence.

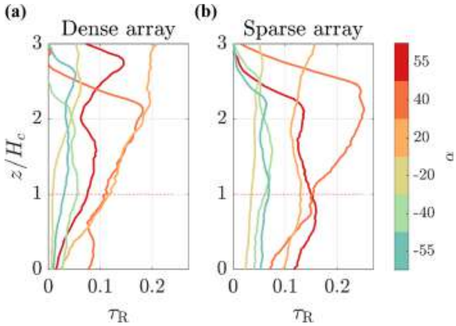

Figure 6. Vertical profiles of the non-dimensional Reynolds stress τ_R, horizontally averaged over the periodic unit for the (a) dense and (b) sparse cases and for varying incidence angle according to the colour scale.

Eventually, figure 6 shows the mean profiles of Reynolds stresses ($\tau_R = -\overline{u'w'}/U^2$), which quantify the momentum transfer driven by turbulent fluctuations and, specifically, the vertical transport of horizontal momentum (Di Bernardino *et al.* 2020*b*). The plots confirm the peculiar role played by the panels, which interact with the incoming flow more like flat airfoil profiles rather than bluff bodies, thereby modifying the structure of the roughness sublayer, Reynolds stresses' magnitude and their vertical distribution, depending on the angle of incidence. There is a clear distinction between positive and negative incidence angles: with $\alpha > 0$, the values of τ_R are consistently higher, compared with the $\alpha < 0$ case, and are generally increasing with height up to $z > 2H_c$. The increase extends over the investigated region (which does not include the full outer boundary layer) in the case $\alpha = +20°$ both in the dense and sparse panel arrangement. In this framework, the turbulent momentum flux is not confined to the immediate canopy interface, as in urban canopies, but extends upward as coherent structures generated at the canopy top grow and interact with the overlying flow (Finnigan 2000; Ghisalberti & Nepf 2002; Raupach *et al.* 1996). In summary, the Reynolds-stress profiles complement the TKE analysis by showing that the enhanced turbulence in the positive incidence cases is associated with an effective vertical transport of streamwise momentum. Conversely, for negative incidence, the weaker canopy-top interaction and the dominance of in-canopy recirculation reduce both turbulence magnitude and momentum exchange.

This analysis suggests that the turbulent momentum transport is more intense when the incidence is positive, correlating with the highest values of TKE, in these conditions. Consequently, the overlying roughness layer experiences a greater degree of vertical mixing and momentum exchange as well as significantly larger TKE in the positive incidence configuration, which can have significant implications for processes such as scalar dispersion, canopy ventilation and energy distribution within the flow. These results are in line with the perspective of Glick *et al.* (2020*a*), where a marked increase in the heat transfer coefficient was observed for large positive incidence. Furthermore, for very large negative incidence, flow structures are similar to those observed in idealised canyons with slender buildings (Badas *et al.* 2020). In the following, we investigate how the instantaneous flow affects ventilation and dispersion and relate it to the turbulent indices here described.

4.3. Canopy ventilation

To quantify ventilation, i.e., the vertical exchange of fluid across the depth of the photovoltaic canopy, we compute the exchange rate

$$\varphi_e(z) = \frac{1}{2Ud}\overline{\int_{\ell(z)} |w(x,z,t)|\,\mathrm{d}x},$$

where $\ell(z)$ is a horizontal line (of length d) across the periodic photovoltaic unit at height z, and the overbar, as usual, denotes time averaging. This non-dimensional index, widely used in urban and planetary

Table 1. *Exchange rate, φ_e, and contribution of the mean flow, φ_{em}, at the canopy top ($z = H_c$), representing the net exchange between the canopy and outer flow*

	α [°]	−55	−40	−20	+20	+40	+55
φ_e (H_c)	$AR = 5/3$	0.0346	0.0337	0.0321	0.0774	0.0608	0.0546
	$AR = 10/3$	0.0445	0.0080	0.0372	0.0799	0.0811	0.0673
φ_{em} (H_c)	$AR = 5/3$	0.0052	0.0066	0.0040	0.0274	0.0061	0.0005
	$AR = 10/3$	0.0082	0.0087	0.0089	0.0391	0.0195	0.0224

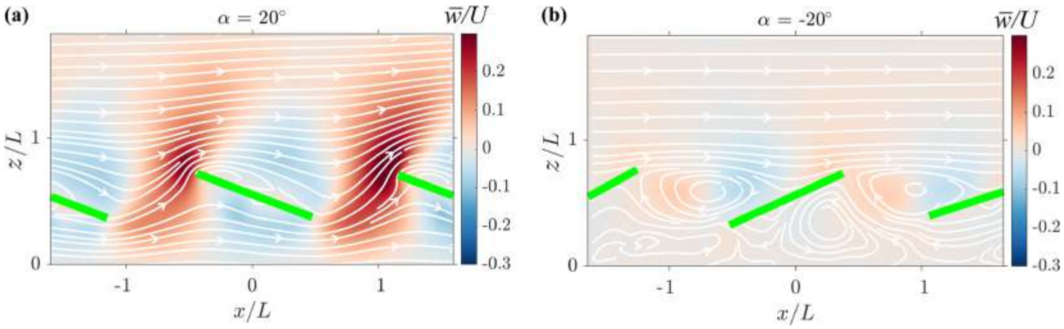

Figure 7. *Streamlines of the mean velocity field overlaid with colour maps of the mean vertical velocity, for the dense case with $\alpha = +20°$ (a) and $-20°$ (b).*

boundary-layer studies, quantifies the volume of fluid exchanged across a horizontal surface per unit surface and time at a given height (Badas *et al*. 2017, 2020; Garau *et al*. 2018). It should be noted that this is the most significant flux in the balance of the periodic photovoltaic unit, since the net flow along the horizontal direction is negligible, provided it is reasonable to assume a well-developed canopy layer since we focus on the 17th downwind periodic unit of the array (Badas *et al*. 2020). Therefore, the upwind flux equals the downwind flux. Evaluating the mass exchange at different heights z is relevant as it can be seen as a measure of the vertical transport within the canopy (Perret *et al*. 2017). Additionally, we computed the sole contribution of the mean flow (figure 7) to ventilation through $\varphi_{em}(z) = \frac{1}{2Ud}\int_{\ell(z)} |\overline{w}(x, z)| \mathrm{d}x$ (Garau *et al*. 2018). First, we analyse the values of φ_e at $z = H_c$, which represents the overall net exchange between the canopy and the overlying roughness layer (table 1).

In the dense panel configuration ($AR = 5/3$) and negative incidence, the exchange rate is low, and its value is $\varphi_e \approx 0.03$, regardless of the angle. Conversely, for positive incidence, φ_e is higher, and decreases from approximately twice to one and a half times the exchange given by the negative incidence, as α increases. This difference agrees with the mean vertical velocity maps shown in figure 7 at $\alpha = \pm 20°$. For positive incidence (figure 7a), the flow exhibits an intense vertical motion across the canopy top, with large positive velocities spanning from the ground to the canopy top and extending into the overlying layer, in the inter-panel gaps. This structure, completely absent with negative α (figure 7b), indicates an active mean contribution to vertical exchange of momentum. In the sparse case ($AR = 10/3$), the exchange rates $\varphi_e(H_c)$ are higher than in the dense configuration, except for the negative incidence angle $\alpha = -40°$, which gives the lowest exchange rate among the investigated configurations. The highest value of the sparse case ($\varphi_e \approx 0.08$) is attained at moderate positive angles ($\alpha = 20°$ and $\alpha = 40°$), a value similar to that of the dense case. Figure 8 presents the vertical profiles of φ_e and φ_{em} as functions of z/H_c. In both cases, negative incidence angles lead to lower exchange rates compared with positive angles. Profiles of the exchange rates qualitatively vary both with incidence and AR: φ_e is only weakly dependent on the incidence, when positive in the lower canopy layer ($z < 0.6H_c$), although a slightly higher dependence is observed for the sparse configuration. The fluid exchange is higher with positive incidence, irrespective of the angle and AR. As concerns φ_{em}, in the AR = *10/3* configuration, a large positive incidence promotes exchange between layers, whereas negative incidence yields profiles similar to those observed in urban

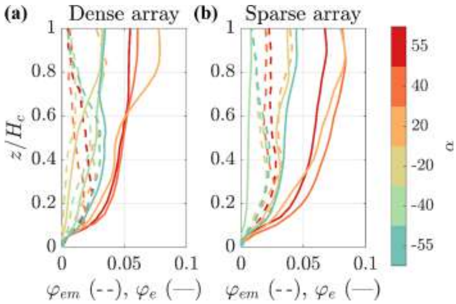

Figure 8. *Vertical profiles of the exchange rate for the two distances and for varying incidence according to the colour scale on the right.*

canyons, characterised by a maximum at mid-height and a decay at the canopy top (Garau *et al*. 2018). In the dense case, all negative angles converge to very similar values at the top, in agreement with the skimming-flow characteristics. The difference between φ_e and φ_{em} increases for the sparse case, highlighting a higher contribution of turbulence to the exchange rate. Eventually, focusing again on φ_e, in the dense case and negative angle, φ_e shows an increasing trend, with higher values close to the canopy top. These trends are analogous to those observed in urban canyons (Garau *et al*. 2018).

In summary, in the sparse case and for positive incidence, the periodic flow expansions between the panels and the ground generate high-momentum, continuous vertical turbulent transport throughout the canopy. The high *TKE* levels observed in these cases agree with the large differences between φ_e and φ_{em}, the signature of a primary role of turbulent fluctuations in the air exchange. Conversely, in the dense configuration and for large incidence (both positive and negative), a skimming flow with reduced mixing at the canopy top develops. These findings indicate that even small positive incidence angles can transform the canopy into an actively ventilated space, driven by continuous, panel-induced vertical turbulent transport. In contrast, a negative incidence establishes the weaker exchange between the canopy and the overlying boundary layer typical of skimming flows (Badas *et al*. 2020, 2021). Even a modest positive incidence can substantially enhance exchange efficiency, promote moisture dispersion and improve thermal regulation in photovoltaic farms. It should be noted that φ_e does not account for flow topology or trapping within recirculation regions, aspects that are accounted for in Section 5 by a Lagrangian analysis, specifically aimed at describing renewal and residence effects within the photovoltaic canopy.

5. Lagrangian dispersion of synthetic particles and turbulent dispersion coefficient

We perform a Lagrangian analysis of dispersion designed to describe the mixing of a passive tracer released close to the ground. To this end, for each experiment, we tracked 50 instantaneous releases of 10,000 synthetic particles, initially homogeneously distributed along a horizontal line at a height of $z_s = h/4$ and passively advected by integrating the instantaneous velocity field using a predictor–corrector algorithm. This choice is intended to be representative of a near-ground source of heat, moisture, pollen or other scalars, released by the soil or vegetation (Moretta *et al*. 2025; Suttie 2000). The region of interest is centred on a panel, with periodic boundary conditions imposed at the boundaries of the periodic unit. The particle and release number was verified to be high enough to attain statistical convergence. Similarly, to obtain statistically meaningful results, the simulation was advanced for 15,000 frames corresponding to 364 L/U (with $L/U = 0.125$ s), for each release. To this aim, the measured instantaneous velocity fields have been used cyclically in time during the integration. The time interval between the releases was heuristically set, after some preliminary tests, to 2.4 L/U to fully capture the sensitivity to initial conditions of the particle trajectories that characterise the turbulent flows, from a Lagrangian

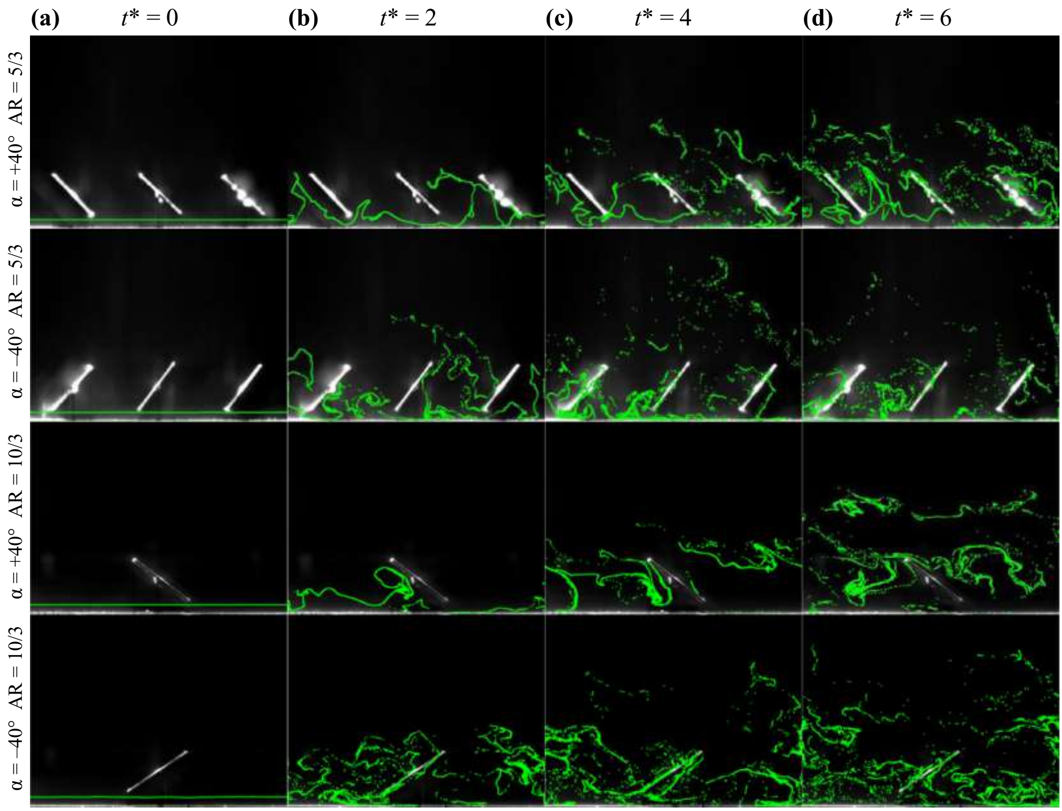

Figure 9. *Synthetic particle (green dots) dispersion in the cases of incidence angles $\alpha = \pm 40°$ at non-dimensional times $t^* = 0, 2, 4, 6$. Particle trajectories are obtained by integrating instantaneous velocity fields starting from a horizontal homogeneous distribution at $z = 0.25h$.*

perspective. Figure 9 shows particles at non-dimensional times $t^* = 0, 2, 4, 6$, with $t^* = t\,U/L$ at incidence angle $\alpha = \pm\, 40°$ for both the investigated panel spacings.

The differences in the dispersion, mainly between the cases with positive and negative angles, are apparent, and can be appreciated more in the Supplementary Videos 1–4. To quantify the exchanges between the photovoltaic canopy and the overlying boundary layer, we then compute the fraction of particles remaining beneath the panels ($z < H_c$) as a function of time, averaged over all releases, $N_b{}^*(t^*)$ (figure 10). For negative incidence angles and both panel spacings, this decay is monotonic. In contrast, large positive incidence cases exhibit non-monotonic behaviours, where an initial decay is followed by one or more reinjections of particles below the panels, highlighting the key role of large-scale coherent structures in the dispersion process. The characteristic time of this reinjection is larger ($t^* \approx 175$) for the dense configuration compared with the sparse configuration ($t^* \approx 150$). The sparse case also exhibits a narrower peak, a signature of a more definite characteristic time. Both the above-mentioned times are too long compared with the advective time across the periodic unit (1.67 L/U and 3.33 L/U, for the dense and sparse configurations, respectively) to be ascribed to the downward periodical deflection of the flow by the panels, also because the latter interpretation would contrast with the characteristic time decrease with AR.

From figures 10a and 10b, we compute the time taken for half of the particles to leave the canopy (i.e., the half-life of $N_{\mathrm{b}}{}^*(t^*)$) rescaled by the advective time scale L/U, which will be denoted as $T_h{}^*$. In the well-mixed box idealisation, $T_h{}^*$ is a proxy of the mean residence time of the particles within the canopy. Results are shown in figure 10c as a function of the incidence angle for the two panel spacings. In agreement with the previous results, negative incidence angles yield longer $T_h{}^*$. The dependence

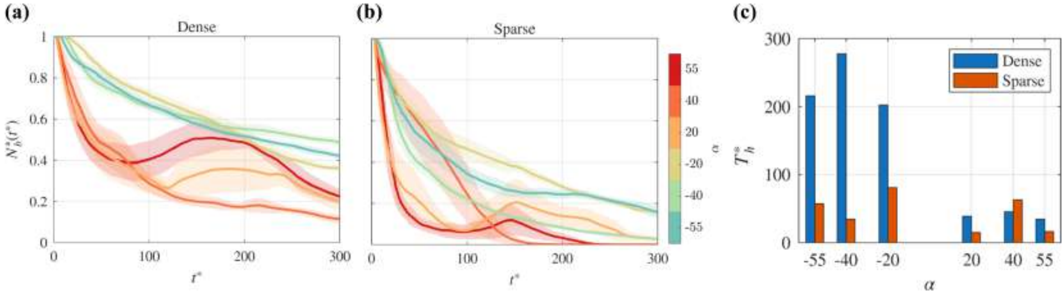

Figure 10. *(a, b) Evolution of the average fraction of particles below the canopy as a function of non-dimensional time. The shaded areas span one standard deviation. (c) Non-dimensional half-life of* $N_b{}^*(t^*)$*,* $T_h{}^*$*, as a function of the incidence angle, α, for the dense and sparse spacings according to the legend.*

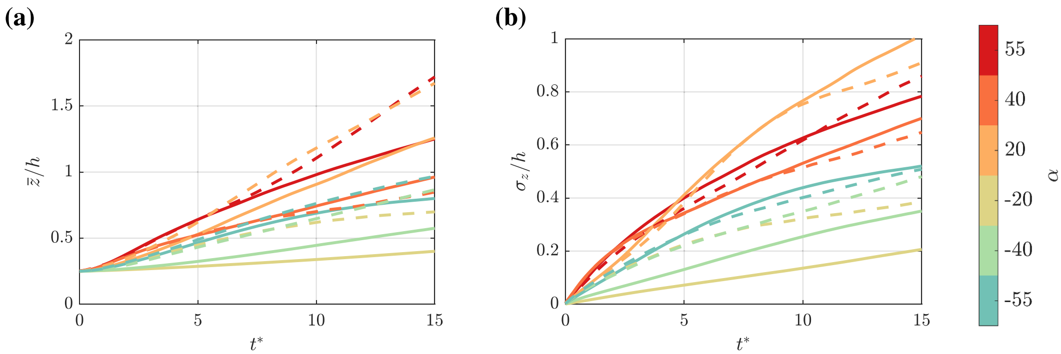

Figure 11. *Mean (a) and standard deviation (b) of synthetic particle height made non-dimensional by h, as functions of non-dimensional time. The colour indicates the incidence angle according to the colour scale on the right. Continuous lines: dense configurations (AR = 5/3); dashed lines: sparse configurations (AR = 10/3).*

on the sign of α is more intense in the dense spacing case, which gives the longest half-life for $\alpha < 0$. In summary, a positive incidence substantially reduces particle residence times beneath the canopy, enhancing ventilation and mixing, while negative incidence cases trap particles for longer periods.

The dispersion from a source close to the ground is described by the statistics of the particle height as a function of time from the release. Specifically, we report the mean particle height, $\overline{z}(t*)/h$, and its standard deviation $\sigma_z(t^*)/h$ (figure 11). The analysis is limited to $t^* = 15$ to avoid biases due to particles exceeding the maximum investigated height. Subsequently, we describe only the initial stage of the dispersion, when the process is dominated by the small-scale turbulence within the canopy. Generally, the behaviour agrees with the above description, with the higher the increase in the average height, the higher the standard deviation (figure 11b). The highest and lowest σ_z curves are given by the dense spacing with $\alpha = \pm 20°$. After an initial linear transient of faster growth due to Lagrangian correlation along particle trajectories, most of the σ_z curves present a square-root behaviour, in agreement with Taylor theory.

Fitting this interval of the non-dimensional standard deviation $\sigma_z(t^*)/h$ with the function $f(t^*) = at^{*1/2} + b$, (being b an arbitrary time shift that accounts for the initial, non-Gaussian, dispersion) allows the non-dimensional turbulent dispersion coefficient within the canopy (i.e., the inverse turbulent Péclet number) to be estimated as $D_T/(LU) = (ah/L)^2/2$. Table 2 reports the inferred values for the investigated cases. For negative incidence, we observe moderate values that monotonically increase as the negative incidence angle increases, with a weak dependence on the distance. For positive incidence, the dispersion

Table 2. *Non-dimensional turbulent dispersion coefficient for the investigated cases*

		$D_T/(LU)$				
α [°]	**−55**	**−40**	**−20**	**20**	**40**	**55**
Dense	0.0147	0.0112	0.0040	0.0801	0.0285	0.0330
Sparse	0.0133	0.0146	0.0052	0.0569	0.0192	0.0579

coefficients are much higher, with a greater dependence on the distance. In that case, high values are observed for $\alpha = 20°$, regardless of the distance, whereas they decrease for $\alpha = 40°$ to increase again at $\alpha = 55°$. For comparison, in water-channel urban-canopy experiments, Di Bernardino *et al.* (2018) obtained $D_T/(\mathrm{LU}) \sim 10^{-3} - 10^{-1}$. The present values, $D_T/(LU) = 4 \times 10^{-3} - 8 \times 10^{-2}$ fall within the same non-dimensional range, with negative incidence corresponding to the lower, skimming-like limit and positive incidence to the upper, shear-layer-dominated limit.

6. Discussion and conclusion

We experimentally investigated the effect of panel incidence and inter-panel distance on the fluid dynamic mechanisms governing flow, turbulence and scalar transport within and above a two-dimensional array of rectangular panels mimicking photovoltaic and agrivoltaic farms. We reproduced the flow in a controlled water channel. Time-resolved measurements of the velocity field were obtained via high-speed imaging and PIV. Two distinct flow regimes emerged as a function of panel inclination. Positive incidence angles promoted enhanced ventilation and mixing across the canopy interface. This behaviour was driven by the development of a strong shear layer and coherent vortical structures above the panels, which enhanced vertical momentum exchange and TKE propagation into the roughness layer. In the dense case, the high-TKE layer was limited at the top of the canopy while, in the sparse case, it propagated at higher heights. Even modest positive angles (*e.g.*, $\alpha = 20°$) were sufficient to generate continuous streamwise jets beneath the panels and upward transport through the canopy top, resulting in exchange rates up to an order of magnitude higher than those observed under negative incidence. Conversely, negative incidence angles induced a skimming-flow regime characterised by large recirculation bubbles confined within the photovoltaic canyon. This configuration suppressed vertical exchange with the overlying flow, yielding low-TKE values and minimal Reynolds stress throughout the canopy depth, regardless of the angle and spacing. The resulting weak ventilation implies longer residence times for passive scalars and suggests reduced capacity for thermal regulation, which may adversely affect microclimatic conditions in agrivoltaic farms.

Panel spacing exerted a secondary, yet non-negligible, influence on velocity field structure. The sparse configuration ($AR = 10/3$) generally enhanced vertical transport compared with the dense arrangement ($AR = 5/3$), particularly under positive incidence, since wider spaces can accommodate high-momentum vertical transport and reduce blockage effects. However, the two-regime scenario remained robust, indicating that the incidence angle is the dominant control parameter for ventilation efficiency in the studied range of parameters. This observation has practical implications for agrivoltaic design: while increasing inter-row distance can improve mixing, the strong dependence on the panel tilt highlights the importance of carefully assessing the mutual orientation between the dominant winds and the panels.

The Lagrangian dispersion analysis reinforced these conclusions by quantifying particle residence times and estimating turbulent dispersion coefficients within the canopy. Positive incidence angles markedly accelerated scalar dispersion and promoted intermittent reinjection events associated with large-scale coherent structures, whereas negative angles trapped particles in the photovoltaic canopy for extended periods. We estimated turbulent dispersion coefficients, which can be helpful when performing RANS simulations or microclimate modelling. Their values further highlighted the sensitivity of mixing processes to panel inclination, with values for positive angles exceeding those for negative angles by more than one order of magnitude.

Overall, this study establishes a fluid mechanical basis for understanding and predicting ventilation and dispersion in photovoltaic canopies. The results highlight that the incidence angle is critical for mixing and photovoltaic canopy ventilation. However, we observed that even small positive inclinations can transform the canopy from a poorly ventilated, recirculation-dominated environment into an actively mixed layer, thereby affecting heat dissipation, moisture and pollen dispersion. These findings are relevant to the optimisation of agrivoltaic farms, where microclimate control is critical for crop productivity and energy efficiency. Furthermore, measurements extending farther above the canopy would make it possible to characterise the full boundary layer and the associated roughness parameters, complementing the picture developed here. Similarly, dedicated analyses of the streamwise development of the internal boundary layer and how it is affected by the change in the angle of incidence and panel array density would complement the present analysis and provide a comprehensive description of photovoltaic canopy turbulence. Future work should extend this analysis to include buoyancy effects and atmospheric stratification (Zhao *et al*. 2021), as well as explore three-dimensional configurations and dynamic anti-tracking systems (Grubbs *et al*. 2024), canopy vegetation (Barwise & Kumar 2020) and the hydrological balance, to fully capture the complexity of real-world photovoltaic farms and, eventually, develop predictive tools for design across diverse climates and crop systems (Amaducci *et al*. 2018).

Supplementary material. Supplementary videos showing the dispersion of synthetic particles described in Section 5 can be found at https://doi.org/10.1017/flo.2026.10063.

Acknowledgements. The authors are grateful to Alessandro Seoni, Antonio Mascia and Omar Pittau for the technical help in setting up and running the experiments.

Data availability statement. The data that support the findings of this study are available from the corresponding author upon reasonable request.

Author contribution. P.G.L.: conceptualisation, methodology, software, formal analysis, investigation, visualisation, writing – original draft, writing – review and editing. M.G.B.: conceptualisation, methodology, formal analysis, writing – review and editing. G.Q.: conceptualisation, methodology, investigation, visualisation, writing – review and editing, supervision. All authors approved the final submitted draft.

Funding statement. This work has been developed within the framework of the project e.INS- Ecosystem of Innovation for Next Generation Sardinia (cod. ECS 00000038) funded by the Italian Ministry for Research and Education (MUR) under the National Recovery and Resilience Plan (NRRP) - MISSION 4 COMPONENT 2, ‘From research to business’ INVESTMENT 1.5, ‘Creation and strengthening of Ecosystems of innovation’ and construction of ‘Territorial R&D Leaders’.

Competing interests. None.

References

Amaducci, S., Yin, X., & Colauzzi, M. (2018). Agrivoltaic systems to optimise land use for electric energy production. *Applied Energy*, *220*, 545–561. https://doi.org/10.1016/j.apenergy.2018.03.081

Badas, M. G., Ferrari, S., Garau, M., & Querzoli, G. (2017). On the effect of gable roof on natural ventilation in two-dimensional urban canyons. *Journal of Wind Engineering and Industrial Aerodynamics*, *162*, 24–34. https://doi.org/10.1016/j.jweia.2017.01.006

Badas, M. G., Ferrari, S., Garau, M., Seoni, A., & Querzoli, G. (2020). On the flow past an array of two-dimensional street canyons between slender buildings. *Boundary-Layer Meteorology*, *174*, 251–273. https://doi.org/10.1007/s10546-019-00484-x

Badas, M. G., Garau, M., & Querzoli, G. (2021). How gable roofs change the mechanisms of turbulent vertical momentum transfer: A LES study on two-dimensional urban canyons. *Journal of Wind Engineering and Industrial Aerodynamics*, *209*, 104432. https://doi.org/10.1016/j.jweia.2020.104432

Barron-Gafford, G. A., Minor, R. L., Allen, N. A., Cronin, A. D., Brooks, A. E., & Pavao-Zuckerman, M. A. (2016). The photovoltaic heat island effect: Larger solar power plants increase local temperatures. *Scientific Reports*, *6*, 35070. https://doi.org/10.1038/srep35070

Barwise, Y., & Kumar, P. (2020). Designing vegetation barriers for urban air pollution abatement: A practical review for appropriate plant species selection. *NPJ Climate and Atmospheric Science*, *3*, 12. https://doi.org/10.1038/s41612-020-0115-3

Bentham, T., & Britter, R. (2003). Spatially averaged flow within obstacle arrays. *Atmospheric Environment*, *37*, 2037–2043. https://doi.org/10.1016/S1352-2310(03)00123-7

Besalduch, L. A., Badas, M. G., Ferrari, S., & Querzoli, G. (2013). Experimental studies for the characterization of the mixing processes in negative buoyant jets. *EPJ Web of Conferences*, *45*, 01012. https://doi.org/10.1051/epjconf/20134501012

Britter, R. E., & Hanna, S. R. (2003). Flow and dispersion in urban areas. *Annual Review of Fluid Mechanics*, *35*, 469–496. https://doi.org/10.1146/annurev.fluid.35.101101.161147

Di Bernardino, A., Monti, P., Leuzzi, G., & Querzoli, G. (2015). Water-channel study of flow and turbulence past a two-dimensional array of obstacles. *Boundary-Layer Meteorology*, *155*, 73–85. https://doi.org/10.1007/s10546-014-9987-2

Di Bernardino, A., Monti, P., Leuzzi, G., & Querzoli, G. (2018). Pollutant fluxes in two-dimensional street canyons. *Urban Climate*, *24*, 80–93. https://doi.org/10.1016/j.uclim.2018.02.002

Di Bernardino, A., Monti, P., Leuzzi, G., & Querzoli, G. (2020a). Turbulent Schmidt number measurements over three-dimensional cubic arrays. *Boundary-Layer Meteorology*, *174*, 231–250. https://doi.org/10.1007/s10546-019-00482-z

Di Bernardino, A., Monti, P., Leuzzi, G., & Querzoli, G. (2020b). Eulerian and Lagrangian time scales of the turbulence above staggered arrays of cubical obstacles. *Environmental Fluid Mechanics*, *20*, 987–1005. https://doi.org/10.1007/s10652-020-09736-8

Dinesh, H., & Pearce, J. M. (2016). The potential of agrivoltaic systems. *Renewable and Sustainable Energy Reviews*, *54*, 299–308. https://doi.org/10.1016/j.rser.2015.10.024

Dupraz, C., Marrou, H., Talbot, G., Dufour, L., Nogier, A., & Ferard, Y. (2011). Combining solar photovoltaic panels and food crops for optimising land use: Towards new agrivoltaic schemes. *Renewable Energy*, *36*, 2725–2732. https://doi.org/10.1016/j.renene.2011.03.005

Fellini, S., Ridolfi, L., & Salizzoni, P. (2020). Street canyon ventilation: Combined effect of cross-section geometry and wall heating. *Quarterly Journal of the Royal Meteorological Society*, *146*, 2347–2367. https://doi.org/10.1002/qj.3795

Fellini, S., Salizzoni, P., & Ridolfi, L. (2021). Vulnerability of cities to toxic airborne releases is written in their topology. *Scientific Reports*, *11*, 23029. https://doi.org/10.1038/s41598-021-02403-y

Fernando, H. J. S., Lee, S. M., Anderson, J., Princevac, M., Pardyjak, E., & Grossman-Clarke, S. (2001). Urban fluid mechanics: Air circulation and contaminant dispersion in cities. *Environmental Fluid Mechanics*, *1*, 107–164. https://doi.org/10.1023/A:1011504001479

Finnigan, J. (2000). Turbulence in plant canopies. *Annual Review of Fluid Mechanics*, *32*, 519–571. https://doi.org/10.1146/annurev.fluid.32.1.519

Garau, M., Badas, M. G., Ferrari, S., Seoni, A., & Querzoli, G. (2018). Turbulence and air exchange in a two-dimensional urban street canyon between gable roof buildings. *Boundary-Layer Meteorology*, *167*, 123–143. https://doi.org/10.1007/s10546-017-0324-4

Ghisalberti, M., & Nepf, H. M. (2002). Mixing layers and coherent structures in vegetated aquatic flows. *Journal of Geophysical Research*, *107*(C2), 3-1–3-11. https://doi.org/10.1029/2001JC000871

Glick, A., Ali, N., Bossuyt, J., Calaf, M., & Cal, R. B. (2020a). Utility-scale solar PV performance enhancements through system-level modifications. *Scientific Reports*, *10*, 10505. https://doi.org/10.1038/s41598-020-66347-5

Glick, A., Smith, S. E., Ali, N., Bossuyt, J., Recktenwald, G., Calaf, M., & Cal, R. B. (2020b). Influence of flow direction and turbulence intensity on heat transfer of utility-scale photovoltaic solar farms. *Solar Energy*, *207*, 173–182. https://doi.org/10.1016/j.solener.2020.05.061

Grubbs, E. K., Gruss, S. M., Schull, V. Z., Gosney, M. J., Mickelbart, M. V., Brouder, S., Gitau, M. W., Bermel, P., Tuinstra, M. R., & Agrawal, R. (2024). Optimized agrivoltaic tracking for nearly-full commodity crop and energy production. *Renewable and Sustainable Energy Reviews*, *191*, 114018. https://doi.org/10.1016/j.rser.2023.114018

Heusinger, J., Broadbent, A. M., Sailor, D. J., & Georgescu, M. (2020). Introduction, evaluation and application of an energy balance model for photovoltaic modules. *Solar Energy*, *195*, 382–395. https://doi.org/10.1016/j.solener.2019.11.041

Huld, T., Cebecauer, T., Šúri, M., & Dunlop, E. D. (2010). Analysis of one-axis tracking strategies for PV systems in Europe. *Progress in Photovoltaics*, *18*, 183–194. https://doi.org/10.1002/pip.948

Hunter, L. J., Watson, I. D., & Johnson, G. T. (1990). Modelling air flow regimes in urban canyons. *Energy and Buildings*, *15*, 315–324. https://doi.org/10.1016/0378-7788(90)90004-3

Husain, S. Z., Bélair, S., Mailhot, J., & Leroyer, S. (2013). Improving the representation of the nocturnal near-neutral surface layer in the urban environment with a mesoscale atmospheric model. *Boundary-Layer Meteorology*, *147*, 525–551. https://doi.org/10.1007/s10546-013-9798-x

Ledda, P. G., Angius, F., Badas, M. G., & Querzoli, G. (2024). Impact of renewable energy integration: a numerical study of atmospheric flow around models of agrivoltaic farms. In *Int. Conf. Harmon. Atmos. Dispers. Model. Regul. Purp., HARMO. Presented at the 22nd International Conference on Harmonisation within Atmospheric Dispersion Modelling for Regulatory Purposes, HARMO 2024, Harmonisation within Atmospheric Dispersion Modelling for Regulatory Purposes, HARMO*.

Li, B., Lei, C., Zhang, W., Olawoore, V. S., & Shuai, Y. (2024). Numerical model study on influences of photovoltaic plants on local microclimate. *Renewable Energy*, *221*, 119551. https://doi.org/10.1016/j.renene.2023.119551

MacDonald, R. W., Griffiths, R. F., & Cheah, S. C. (1997). Field experiments of dispersion through regular arrays of cubic structures. *Atmospheric Environment*, *31*, 783–795. https://doi.org/10.1016/S1352-2310(96)00263-4

Macdonald, R. W., Griffiths, R. F., & Hall, D. J. (1998). An improved method for the estimation of surface roughness of obstacle arrays. *Atmospheric Environment*, *32*, 1857–1864. https://doi.org/10.1016/S1352-2310(97)00403-2

Moretta, M., Moriondo, M., Rossi, R., Carvalho, G. M. D. C. P., Padovan, G., Dal Prà, A., Palchetti, E., Argenti, G., Staglianò, N., Balingit, A. R., & Leolini, L. (2025). Integrated modelling of shading effects on alfalfa growth across different agrivoltaic systems. *Frontiers in Agronomy*, *7*, 1699126. https://doi.org/10.3389/fagro.2025.1699126

Mouzourides, P., Marakkos, C., & Neophytou, M. K.-A. (2022). Urban street canyon flows under combined wind forcing and thermal buoyancy. *Physics of Fluids*, *34*, 076606. https://doi.org/10.1063/5.0090642

Ngan, K., & Lo, K. W. (2016). Revisiting the flow regimes for urban street canyons using the numerical Green's function. *Environmental Fluid Mechanics*, *16*, 313–334. https://doi.org/10.1007/s10652-015-9422-3

Oke, T. R. (1988). Street design and urban canopy layer climate. *Energy and Buildings*, *11*, 103–113. https://doi.org/10.1016/0378-7788(88)90026-6

Perret, L., Blackman, K., Fernandes, R., & Savory, E. (2017). Relating street canyon vertical mass-exchange to upstream flow regime and canyon geometry. *Sustainable Cities and Society*, *30*, 49–57. https://doi.org/10.1016/j.scs.2017.01.001

Raupach, M. R., Finnigan, J. J., & Brunei, Y. (1996). Coherent eddies and turbulence in vegetation canopies: The mixing-layer analogy. *Boundary-Layer Meteorology*, *78*, 351–382. https://doi.org/10.1007/BF00120941

Reynolds, R. T., & Castro, I. P. (2008). Measurements in an urban-type boundary layer. *Experiments in Fluids*, *45*, 141–156. https://doi.org/10.1007/s00348-008-0470-z

Simón-Moral, A., Santiago, J. L., Krayenhoff, E. S., & Martilli, A. (2014). Streamwise versus spanwise spacing of obstacle arrays: Parametrization of the effects on drag and turbulence. *Boundary-Layer Meteorology*, *151*, 579–596. https://doi.org/10.1007/s10546-013-9901-3

Smith, J. A., Pisetta, G., & Viola, I. M. (2021). The scales of the leading-edge separation bubble. *Physics of Fluids*, *33*, 045101. https://doi.org/10.1063/5.0045204

Smith, S. E., Viggiano, B., Ali, N., Silverman, T. J., Obligado, M., Calaf, M., & Cal, R. B. (2022). Increased panel height enhances cooling for photovoltaic solar farms. *Applied Energy*, *325*, 119819. https://doi.org/10.1016/j.apenergy.2022.119819

Song, J., & Wang, Z.-H. (2015). Interfacing the urban land–Atmosphere system through coupled urban canopy and atmospheric models. *Boundary-Layer Meteorology*, *154*, 427–448. https://doi.org/10.1007/s10546-014-9980-9

Soulhac, L., Salizzoni, P., Cierco, F.-X., & Perkins, R. (2011). The model SIRANE for atmospheric urban pollutant dispersion; part I, presentation of the model. *Atmospheric Environment*, *45*, 7379–7395. https://doi.org/10.1016/j.atmosenv.2011.07.008

Stanislawski, B. J., Harman, T., Silverman, T. J., Cal, R. B., & Calaf, M. (2022). Row spacing as a controller of solar module temperature and power output in solar farms. *Journal of Renewable and Sustainable Energy*, *14*, 063702. https://doi.org/10.1063/5.0123641

Suttie, J. M. (2000). Hay and Straw Conservation: For Small-Scale Farming and Pastoral Conditions, FAO Plant Production and Protection Series. Food and Agriculture Organization of the United Nations.

Uehara, K., Wakamatsu, S., & Ooka, R. (2003). Studies on critical Reynolds number indices for wind-tunnel experiments on flow within urban areas. *Boundary-Layer Meteorology*, *107*, 353–370. https://doi.org/10.1023/A:1022162807729

Vigiak, O., Sterk, G., Warren, A., & Hagen, L. J. (2003). Spatial modeling of wind speed around windbreaks. *CATENA*, *52*, 273–288. https://doi.org/10.1016/S0341-8162(03)00018-3

Zhao, Y., Chew, L. W., Kubilay, A., & Carmeliet, J. (2020). Isothermal and non-isothermal flow in street canyons: A review from theoretical, experimental and numerical perspectives. *Building and Environment*, *184*, 107163. https://doi.org/10.1016/j.buildenv.2020.107163

Zhao, Y., Li, H., Kubilay, A., & Carmeliet, J. (2021). Buoyancy effects on the flows around flat and steep street canyons in simplified urban settings subject to a neutral approaching boundary layer: Wind tunnel PIV measurements. *Science of the Total Environment*, *797*, 149067. https://doi.org/10.1016/j.scitotenv.2021.149067

Cite this article: Ledda P. G., Badas M. G. and Querzoli G. (2026). Turbulent flow past idealised arrays of photovoltaic panels: an experimental study. *Flow*, *6*, E25. https://doi.org/10.1017/flo.2026.10063